Electronic Supplementary Material (ESI) for Journal of Materials Chemistry A.

Supporting Information

Ultrafast Dynamic Response of Waterproof Stretchable Strain Sensors Based on Wrinkle-Templated Microcracking

Lele Li,[#] Yang Zheng,[#] Enping Liu, Juanjuan Wang, Xue Han, Shichun Jiang, Fan Xu, Yanping Cao,* Conghua Lu**

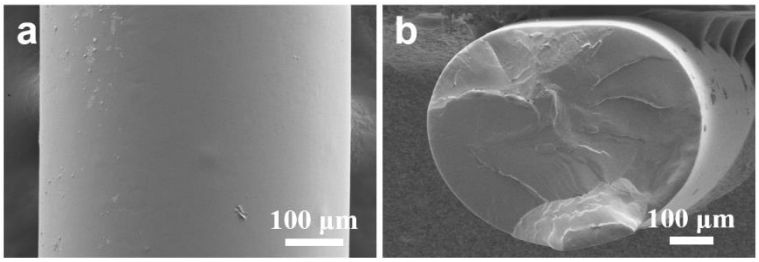

Figure S1. SEM images of surface (a) and cross-section part (b) of the pristine PDMS fiber.

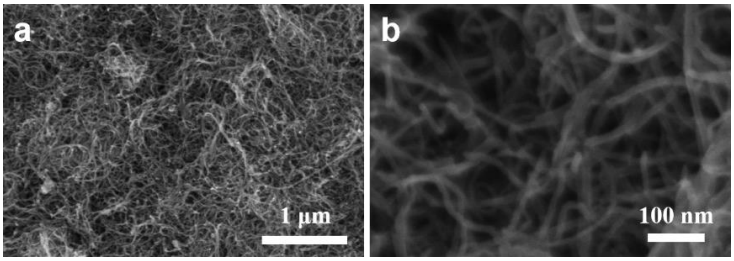

Figure S2. SEM images of the pristine CNTs.

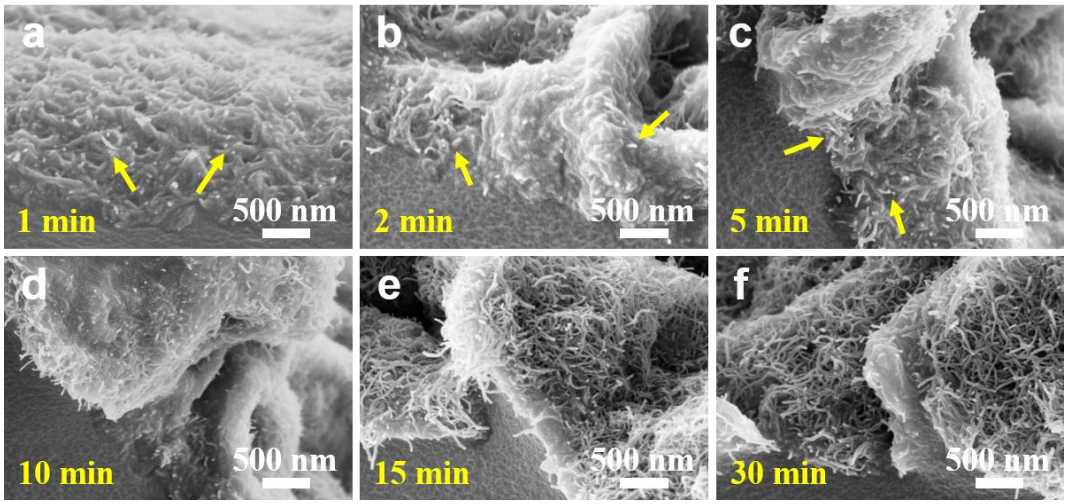

Figure S3. Cross-sectional SEM images of CNTs@PDMS fiber prepared from different ultrasonic durations. The embedded CNTs were marked by yellow arrows.

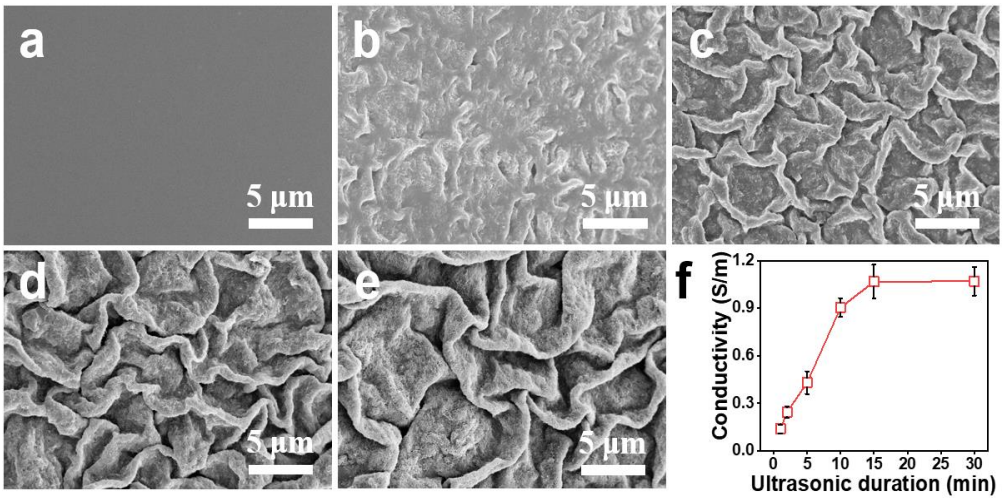

Figure S4. Morphologies and conductivity of CNTs@PDMS fibers. SEM images of CNTs@PDMS fibers from the ultrasonic duration of (a) 0 min, (b) 1 min, (c) 2 min, (d) 10 min, (e) 30 min, respectively. (f) Dependence of conductivity of CNTs@PDMS fibers on the ultrasonic duration.

In the current case, surface wrinkling on the PDMS fiber is induced by solvent swelling. Because the volume expansion of the PDMS fiber is isotropic, a homogeneous compression stress is induced with the resulting labyrinth wrinkling structure on the CNTs/PDMS system. As shown in Figure 1c, some CNTs are protruding out of the PDMS matrix, instead of simply adhering on the PDMS surface. More evidences can be found in the cross-section SEM images shown in Figure S3. When the ultrasonic duration is relatively low (e.g., 1 min, 2 min), we have the opportunity to observe the bonding state of CNTs in the ultrasonic deposition process. It is seen that most of the CNTs are inserted into the PDMS skin and there is no obvious interface between CNTs layer and PDMS matrix. Therefore, the CNTs have good interface bonding strength with PDMS surface, which is different from the composites prepared by spraying or dip coating with the resulting weak interface interaction. Additionally, with the increase of ultrasonic duration from 1 min to 15 min, more and more CNTs were deposited on the PDMS surface (Figure S3). With further increase of ultrasonic duration to 30 min, the amount of the decorated CNTs seems similar to that from ultrasonic duration of 15 min. This indicates that the deposition amount of CNTs has reached a saturation value. The change of the deposition amount of CNTs on the resulting CNTs@PDMS fibers is verified by the evolution of the wrinkling wavelength and conductivity with the ultrasonic duration (Figure S4). It has been concluded that in a case of a small strain imposed, the wrinkling wavelength is determined by:

$$\lambda_0 = 2\pi h \left[\frac{(1-\nu_s^2)E_f}{3(1-\nu_f^2)E_s} \right]^{1/3}$$

where h is the rigid film thickness, E is the Young's modulus, ν is Poisson's ratio. Subscripts f and s refer to the film and substrate. In the current case, the wrinkling

wavelength of the wrinkled CNTs layer can be tailored by adjusting the thickness of the deposited CNTs layer (i.e., the ultrasonic duration). Furthermore, the deposited CNTs are uniformly distributed on the PDMS surface and the corresponding wrinkling wavelength is basically uniform, especially from the macroscopical view (Figure S5). More importantly, the sensing performances from sample to sample for ACPF strain sensors have good reproducibility (Figure S9), further indicating the consistency of different samples and the good repeatability of the fabrication process. This reproducibility comes from the well control of the wrinkling structure and the conductivity of each layer (i.e., CNTs layer and Ag NPs layer) in the curre case.

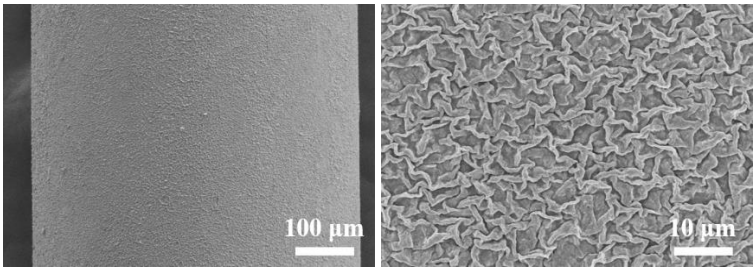

Figure S5. SEM images of CNTs@PDMS fiber at a low magnification. The wrinkle structure is uniform from the macroscopical view.

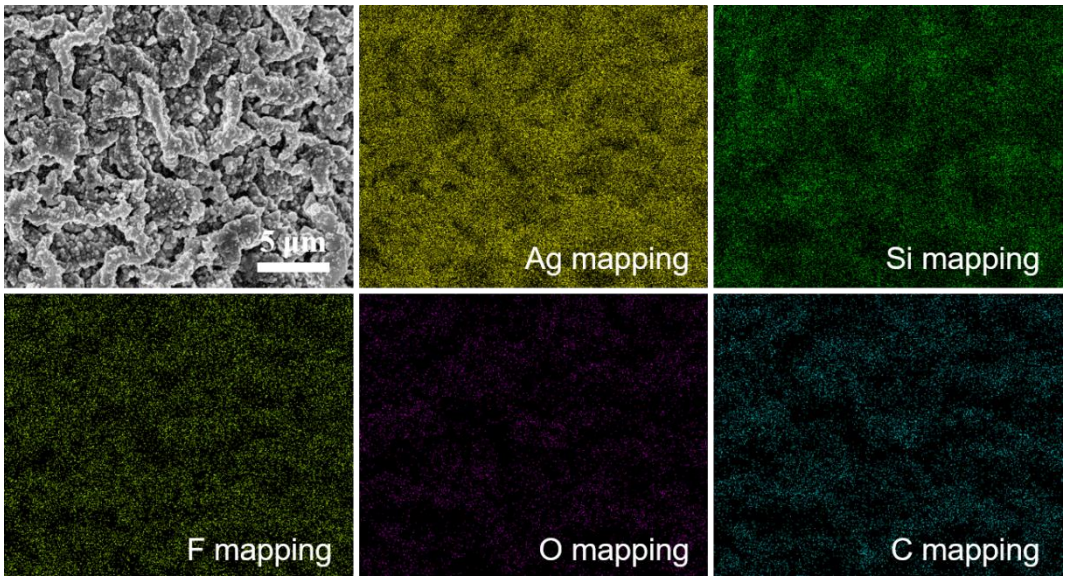

Figure S6. SEM image and the corresponding EDS mapping images of the Ag@CNTs@PDMS fiber (i.e., ACPF).

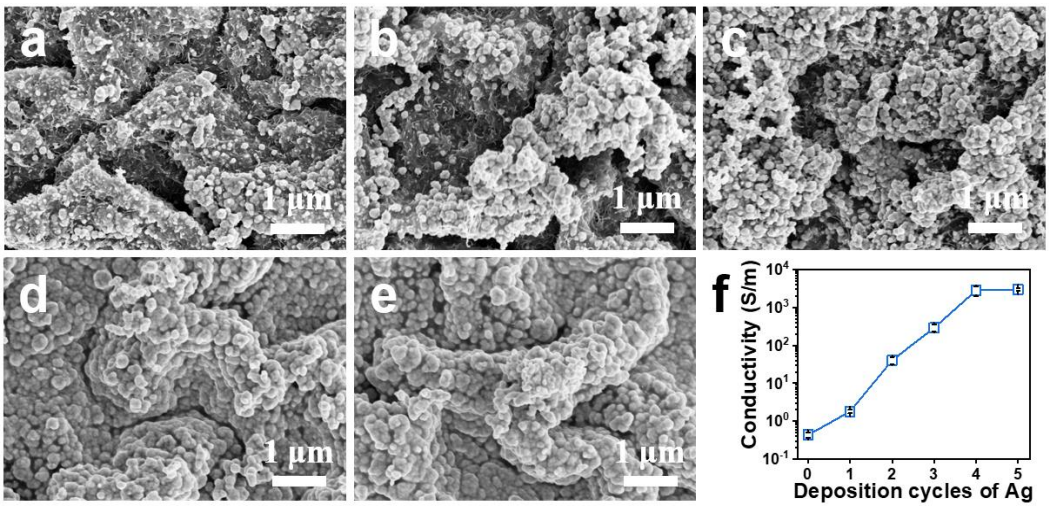

Figure S7. Morphologies and conductivity of ACPF fibers. SEM images of ACPF from different deposition cycles of Ag NPs: (a) 1, (b) 2, (c) 3, (d) 4 and (e) 5, respectively. (f) Dependence of conductivity of ACPF on the deposition cycle of Ag NPs

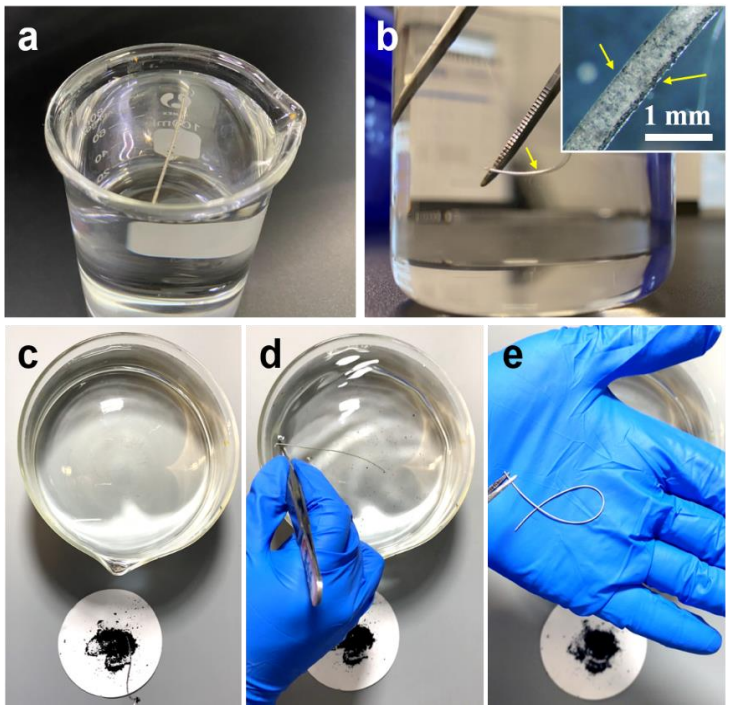

Figure S8. Superhydrophobic and self-cleaning performances of ACPF. (a) The ACPF floats on the water surface like a water strider. (b) After immersing into water, the fiber shows an air layer between the fiber and water. Inset in Frame b shows the optical image of ACPF underwater and the air layer is indicated by the yellow arrows. (c-e) Photographs show that the ACPF was contaminated by the C powder, followed by water washing.

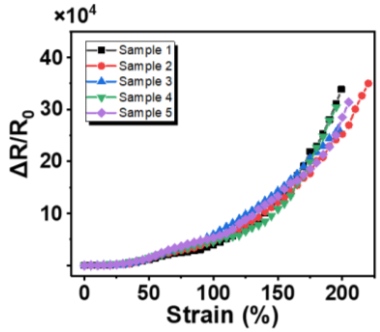

Figure S9. Sample to sample strain-sensing behavior of the ACPF strain sensors

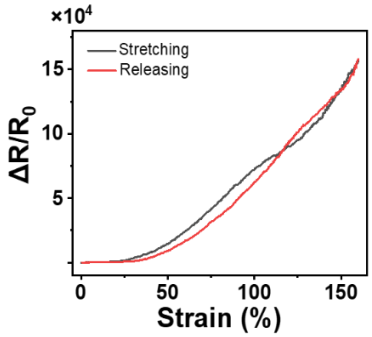

Figure S10. Electrical hysteresis performance of the ACPF strain sensor at the 160% strain.

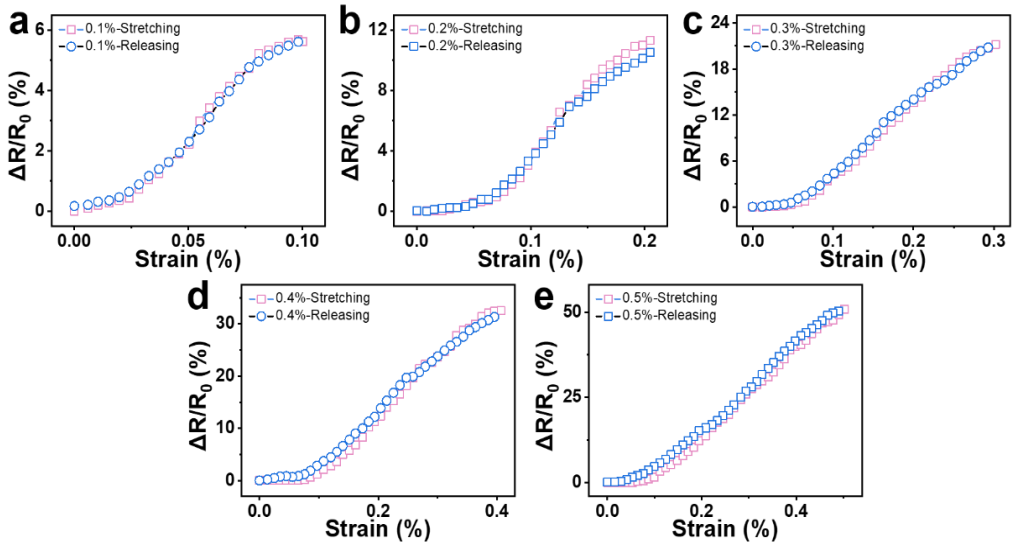

Figure S11. Electrical hysteresis performances of ACPF strain sensors in a subtle strain range: (a) 0.1%, (b) 0.2%, (c) 0.3%, (d) 0.4% and (e) 0.5%, respectively.

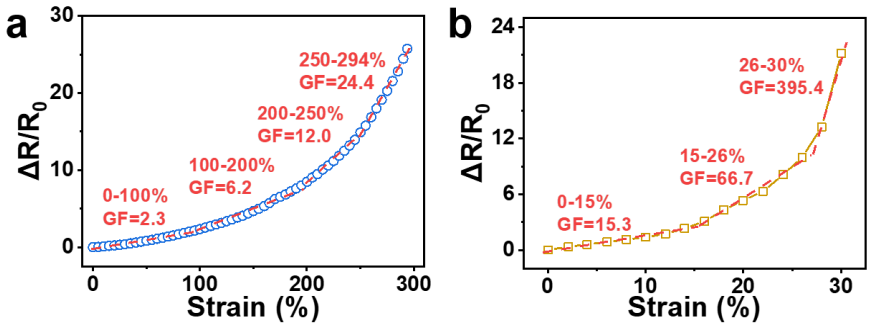

Figure S12. Strain-sensing curve of a CNTs@PDMS fiber strain sensor (a) and a Ag@PDMS fiber strain sensor.

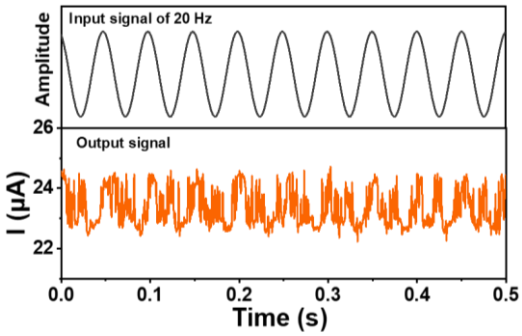

Figure S13. Current response for the CNTs@PDMS fiber strain sensor to a 20 Hz dynamic mechanical stimulus.

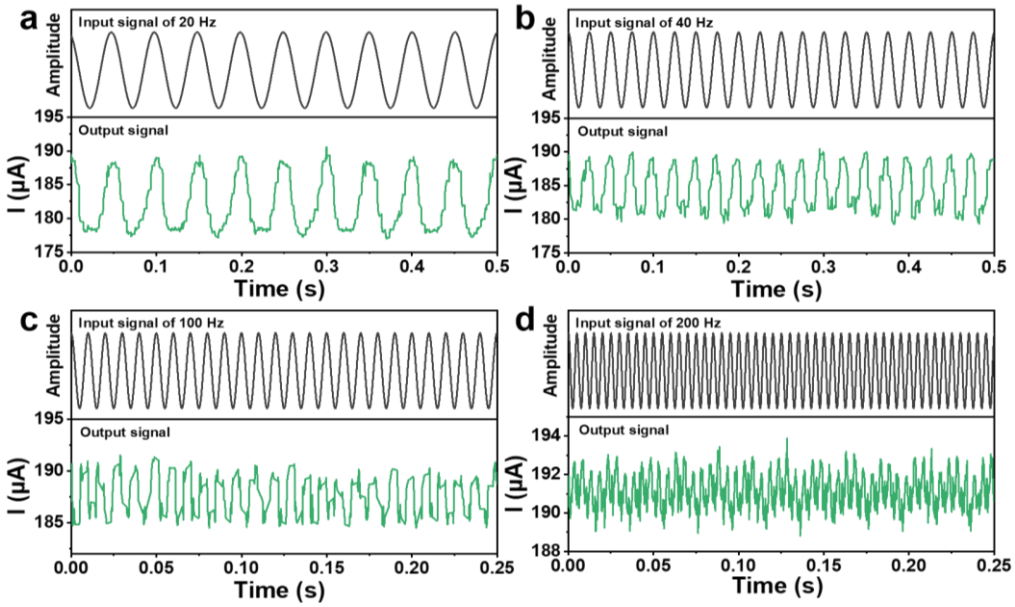

Figure S14. Current responses for a Ag@PDMS fiber strain sensor to dynamic mechanical stimuli with various frequencies: (a) 20 Hz, (b) 40 Hz, (c) 100 Hz and (d) 200 Hz, respectively.

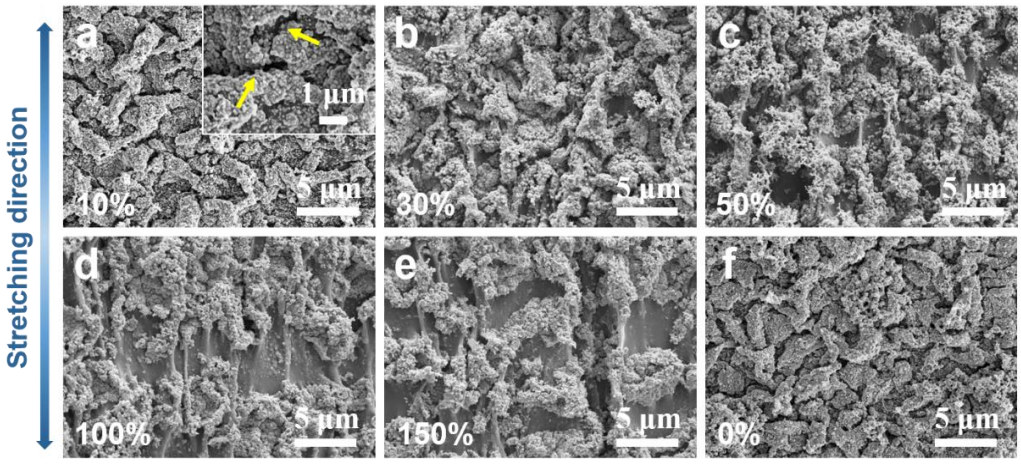

Figure S15. SEM images of ACPF strain sensor under different stretching strains: (a) 10%, (b) 30%, (c) 50%, (d) 100%, (e) 150% and (f) restoring to 0% after releasing the 150% strain. Inset in Frame a is the enlarged SEM image, in which the microcracks were pointed out by yellow arrows.

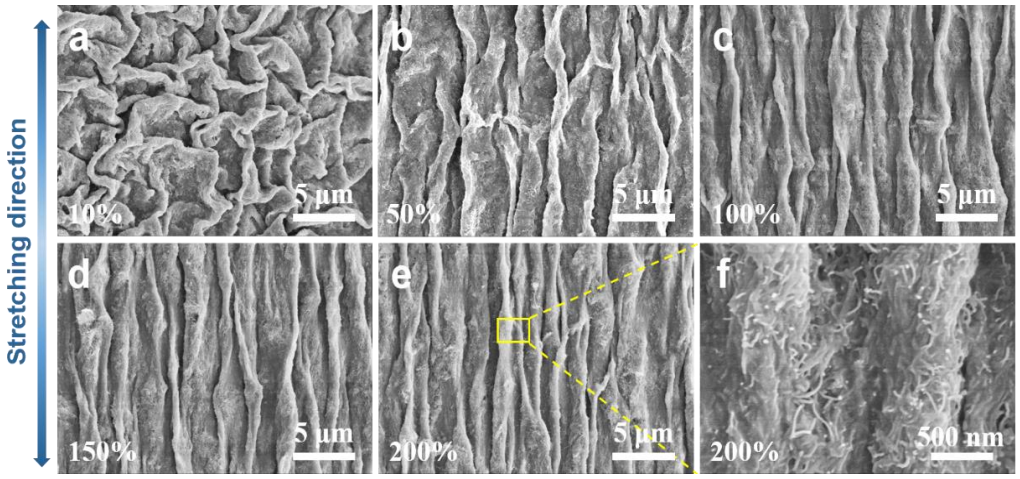

Figure S16. SEM images of the CNTs@PDMS fiber under different strains employed: (a) 10%, (b) 50%, (c) 100%, (d) 150%, and (e, f) 200%, respectively.

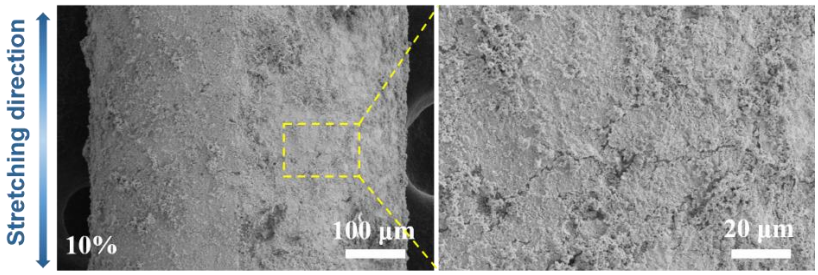

Figure S17. SEM images of the Ag@PDMS fiber under a 10% strain applied.

It is seen that under a small uniaxial strain (e.g., ε =10%), abundant microcracks are induced preferentially along the toughs of the conformal wavy microstructure (Figure S15a), which leads to the prominent resistance change (ε: 0~15%, GF=1700, Figure 2a). With the further increase of the applied strain, the microcracks gradually expand and the microcracking gaps grow significantly (Figure S15b-e). Most of the as-induced microcracks seem perpendicular to the stretching direction when the fiber strain sensor is subjected to a large strain (ε >50%) (Figure S15d,e), in which the electron transport ways along the Ag NPs layer greatly decreases. Even when the fiber strain sensor undergoes a large strain of 150%, some of the underlying CNTs layer is still reserved in the fiber matrix, demonstrating their strong interface bonding strength with the PDMS fiber substrate. After the applied strain is fully released, the microcracks seem to self-heal and the original sinusoidal microstructure is preserved (Figure S15f), endowing the ACPF strain sensor with outstanding stability and reversibility. By contrast, no obvious cracking is observed on the CNTs@PDMS fiber upon stretching from 0 to 200% strain (Figure S16). It is noted that when the applied strain is up to 50%, the labyrinth wrinkling structures are gradually converted into oriented ones (with the orientation parallel to the fiber axis) owing to the Poisson effect. Due to the stress-relief character of the wrinkling morphology, a limited resistance change is induced on the CNTs@PDMS strain sensor during stretching, especially in the small strain range. As a result, the CNTs@PDMS strain sensor has a low sensitivity (ε: 0~100%, GF=2.3, Figure S12a). With respect to the Ag@PDMS fiber, only a few randomly distributed microcracks accompanied with a long microcracking persistence length are induced under the small strain (Figure S17), which is in sharp contrast to the abundant controlled microcracks formed in the ACPF. These insufficient microcracking of the Ag@PDMS fiber is not enough to stimulate a high sensitivity (ε: 0~15%, GF=15.3, Figure S12b).

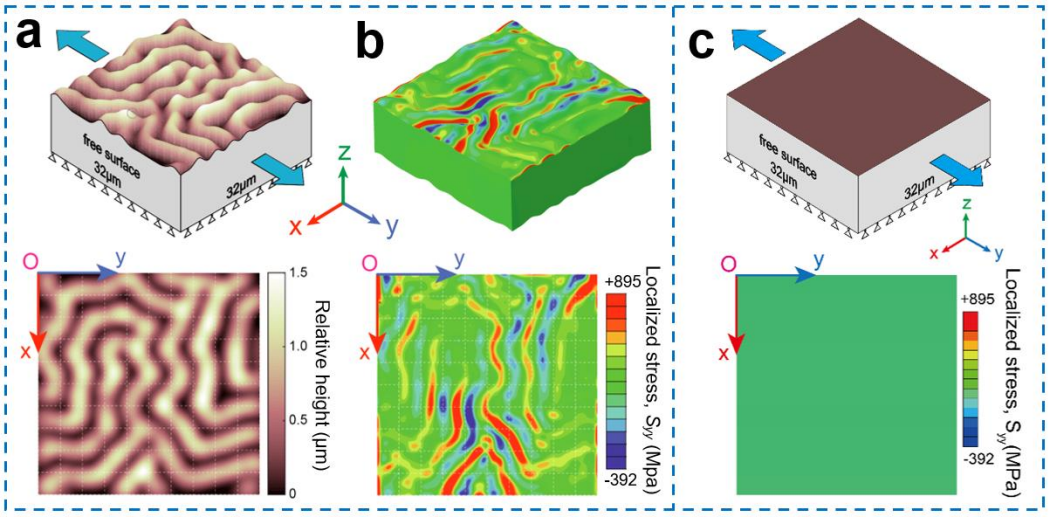

Figure S18. FEA simulation of the ACPF strain sensor. FEM simulation of uniaxial stretching on the Ag@CNT@PDMS trilayer system with a wrinkle surface: (a) Initial configuration of the trilayer model and the relative height distribution of the trilayer surface; (b) S_{yy} distribution of the Ag surface layer under uniaxial stretching. FEM simulation of uniaxial stretching on the trilayer system with a flat surface: (c) Initial configuration of the trilayer; S_{yy} of about 140 MPa was basically uniformly distributed on Ag layer. Only surface pattern was set different between the above two simulations. Color bar of S_{yy} in these two simulations were consistent for comparison.

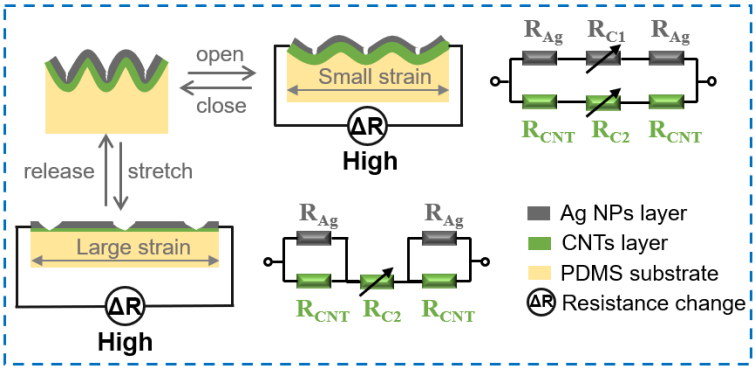

Figure S19. Schematic illustration of the conducting mechanism and the corresponding equivalent circuits of the ACPF strain sensor under small and large strains, respectively.

Based on the above morphology evolution and strain-sensing results, an equivalent circuit model for the bilayer fiber strain sensor is also established. As demonstrated in Figure S19, the total equivalent electrical resistance (R_{total}) of the ACPF strain sensor can be simplified as two conductive layers in the parallel configuration. When a relatively small strain range (ε: 0~50%) is loaded, the susceptible Ag NPs surface-layer microcracks in a controlled manner, whereas, the as-wrinkled CNTs interlayer accommodates the strain through the stress-relief structural deformation. Considering the huge difference in the conductivity of the Ag NPs/CNTs bilayer, the

prominent decrease in conductivity is mainly ascribed to the as-formed Ag NPs microcracks. Upon removing the external strain, the microcracks promptly close with the assistance of the recovery of wrinkling structure. On account of the rapidly open and close behaviors of the abundant microcracks upon straining, the ACPF strain sensor demonstrates the ultrahigh sensitivity and ultrafast response behaviors. These results further prove that the wrinkling structure and the wrinkle-templated surface microcracking are responsible for the excellent dynamic sensing performances in the subtle strain range. When the applied strain surpasses the stored pre-strain (in the current case, ε = 50%), the entangled CNTs still remain interconnected. Thus the CNTs interlayer takes charge of the sensing transducer role in the large strain, further boosting the sensitivity and stretchability of the ACPF strain sensor through the slippage of the entangled CNTs. As a consequence, the ACPF strain sensor maintains remarkable stretchability and outstanding sensitivity no matter in the small or large strain ranges.

It is noted that the thickness of the conformal Ag NPs surface-layer and the wrinkled CNTs interlayer is directly related to respective initial conductivity of each layer (Figure S4f, S7f). According to the analysis of wrinkle-templated microcracking mechanism, we see that the initial conductivity of Ag NPs layer and CNTs layer plays a key role in boosting the sensitivity of ACPF strain sensor, especially in the small strain range (e.g., ε < 50%). Because the as-wrinkled CNTs interlayer is insensitive to the applied small strain (GF=2.3 within 0~100% strain, Figure S12a) and the conductivity of CNTs layer (0.43 S/m) is much lower than that of Ag NPs layer (2990 S/m), the sharp decrease in the conductivity of ACPF strain sensor should be attributed to the dramatic increase of R_{C1} caused by the as-formed Ag NPs microcracks. Additionally, gauge factor ($GF = \delta(\Delta R / R_0) / \delta_\varepsilon$) is employed to quantitatively evaluate the sensitivity of strain sensors. Thus the R_0 decrease and the ΔR increase will lead to a high GF. If we don't take the wrinkle morphology and mechanical factors into consideration, the larger the initial conductivity difference between Ag NPs surface-layer and CNTs interlayer, the lower R_0 and the higher ΔR will be obtained, leading to a higher GF. If the conductivity of the CNTs layer is close to or higher than the Ag NPs layer, the microcrack-induced R_{C1} change will not cause the significant R_{total} change, leading to a low sensitivity in the small strain range. Therefore, in order to enhance the sensitivity of ACPF strain sensor, we can modulate the initial conductivity difference between Ag NPs surface-layer and CNTs interlayer that are just corresponding to the thickness of each layer.

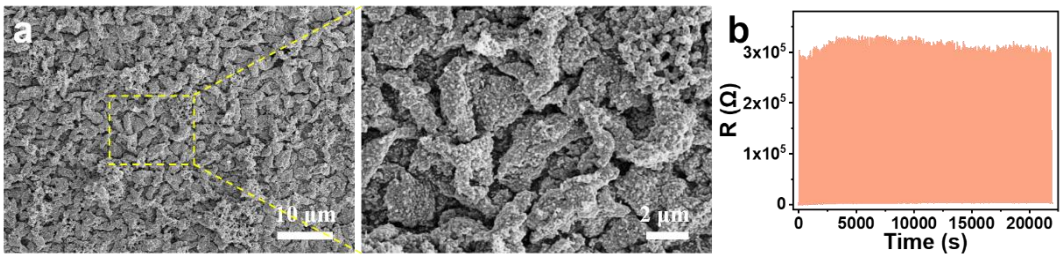

Figure S20. (a) SEM images of ACPF after 200 stretching/releasing cycles under the 60% strain employed. (b) Durability test of the ACPF strain sensor for 200 cycles under the 60% strain employed.

The as-wrinkled CNTs interlayer may act as a mechanical buffer layer to alleviate the mechanical mismatch between the rigid Ag NPs layer and the elastic PDMS fiber, preventing the Ag NPs layer from delaminating. As a result, the bilayer conductive networks can retain the structural integrity (Figure S17) and strain-sensing stability even after undergoing cyclic loading/unloading of a large strain.

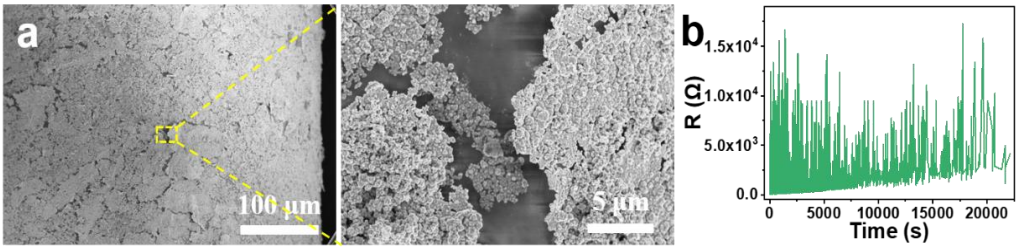

Figure 21. (a) SEM images of the Ag@PDMS fiber after 200 stretching/releasing cycles under the 60% strain employed. (b) Durability test of the Ag@PDMS fiber strain sensor for 200 cycles under the 60% strain employed.

By contrast, the Ag@PDMS fiber strain sensor gradually losses the strain response owing to the as-induced irreversible delamination and film breakage under the same conditions.

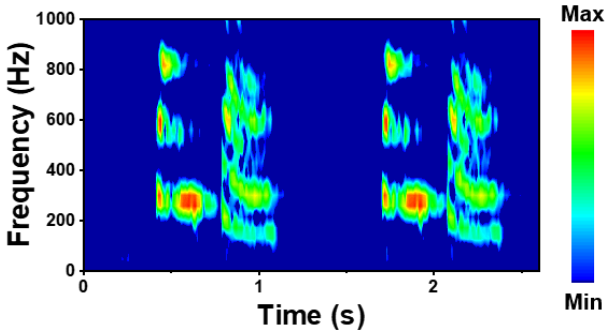

Figure S22. Spectrogram for phonation of "sensor" twice recorded by a reference microphone.

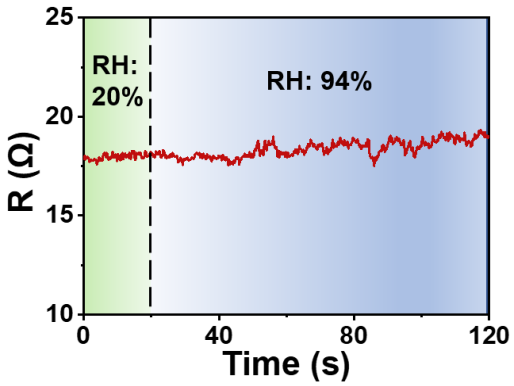

Figure S23. Influence of humidity on the conductivity performance of the ACPF strain sensor.

Table S1. Comparison of dynamic sensing performances of the current strain sensor with other strain sensors reported in the literature.

Materials	Max GF	Max stretchability	Response time (ms)	Detectable frequency (Hz)	Superhydrophobicity / Underwater dynamic sensing	Ref.
CB/PDMS/P3HT/PU fiber	863	400%	51	0.3	No	[1]
Ag NWs/WPU-MXene fiber	1.6×10^{7}	100%	344	0.4	No	[2]
Ag NWs/acrylate/PDMS film	10486	20%	14.4	1	No	[3]
CNTs/PU fiber	1344	200%	88	1	No	[4]
rGO/PDMS/VHB film	167665	300%	90	2.5	Yes*	[5]
CNTs/Ecoflex film	13.5	550%	33	8	No	[6]
Pt/PUA film	2000	2%	N/A	659	No	[7]
CB/PAA/ ethyl cellulose film	647	0.22%	0.625	800	No	[8]
Au/PDMS film	5000	1%	N/A	988	No	[9]
Vertical graphene/PDMS film	22000	100%	N/A	2 500	No	[10]
Vertical aligned-Au NWs/Ecoflex film	N/A	N/A	N/A	3 000	No	[11]
rGO/PDMS film	8699	1%	0.107	20 000	Yes*	[12]
Conductive ink/paper	18300	0.2%	8	N/A	Yes*	[13]
SiO_2/CB/PDMS/CIP	354	250%	N/A	N/A	Yes*	[14]
Ag NPs/CNTs/PDMS fiber	**4.4×10^{5}**	**200%**	**0.08**	**20 000**	**Yes**	**This work**

*: The reported waterproof strain sensors haven't concerned about the underwater dynamic sensing performances.

Table S2. Mechanical performances of different fibers in this work.

Materials	Tensile strength (MPa)	Young's modulus (kPa)	Elongation at breakage (%)
Pure PDMS fiber	4.37±0.19	590±26	303±14
CNTs@PDMS fiber	4.95±0.26	681±50	300±15
ACPF	4.06±0.28	836±52	211±11

Table S3. Material parameters and each layer thickness in ACPF for simulation.

Materials	Thickness	Young's Modulus	Poisson's Ratio
PDMS	10 μm	0.62 MPa	0.48
CNTs	30 nm	500 GPa	0.19
Ag	100 nm	83 GPa	0.37

References

[1] S. Jang, J. Kim, D. W. Kim, J. W. Kim, S. Chun, H. J. Lee, G. R. Yi, C. Pang, Carbon-based, ultraelastic, hierarchically coated fiber strain sensors with crack-controllable beads. *ACS Appl. Mater. Interfaces* **2019**, *11*, 15079-15087.

[2] J. H. Pu, X. Zhao, X. J. Zha, L. Bai, K. Ke, R. Y. Bao, Z. Y. Liu, M. B. Yang, W. Yang, Multilayer structured AgNW/WPU-MXene fiber strain sensors with ultrahigh sensitivity and a wide operating range for wearable monitoring and healthcare. *J. Mater. Chem. A* **2019**, *7*, 15913-15923.

[3] G. S. Liu, F. Yang, J. Xu, Y. Kong, H. Zheng, L. Chen, Y. Chen, M. X. Wu, B. R. Yang, Y. Luo, Z. Chen, Ultrasonically patterning silver nanowire-acrylate composite for highly sensitive and transparent strain sensors based on parallel cracks. *ACS Appl. Mater. Interfaces* **2020**, *12*, 47729-47738.

[4] H. Sun, K. Dai, W. Zhai, Y. Zhou, J. Li, G. Zheng, B. Li, C. Liu, C. Shen, A highly sensitive and stretchable yarn strain sensor for human motion tracking utilizing a wrinkle-assisted crack structure. *ACS Appl. Mater. Interfaces* **2019**, *11*, 36052-36062.

[5] Z. Chu, W. Jiao, Y. Huang, Y. Zheng, R. Wang, X. He, Superhydrophobic gradient wrinkle strain sensor with ultra-high sensitivity and broad strain range for motion monitoring. *J. Mater. Chem. A* **2021**, *9*, 9634-9643.

[6] B. Liang, Z. Lin, W. Chen, Z. He, J. Zhong, H. Zhu, Z. Tang, X. Gui, Ultra-stretchable and highly sensitive strain sensor based on gradient structure carbon nanotubes. *Nanoscale* **2018**, *10*, 13599-13606.

[7] D. Kang, P. V. Pikhitsa, Y. W. Choi, C. Lee, S. S. Shin, L. Piao, B. Park, K. Y. Suh, T. I. Kim, M. Choi, Ultrasensitive mechanical crack-based sensor inspired by the spider sensory system. *Nature* **2014**, *516*, 222-226.

[8] H. Song, J. Zhang, D. Chen, K. Wang, S. Niu, Z. Han, L. Ren, Superfast and high-sensitivity printable strain sensors with bioinspired micron-scale cracks. *Nanoscale* **2017**, *9*, 1166-1173.

[9] T. Yang, X. Li, X. Jiang, S. Lin, J. Lao, J. Shi, Z. Zhen, Z. Li, H. Zhu, Structural engineering of gold thin films with channel cracks for ultrasensitive strain sensing. *Mater. Horiz.* **2016**, *3*, 248-255.

[10] C. Deng, P. Gao, L. Lan, P. He, X. Zhao, W. Zheng, W. Chen, X. Zhong, Y. Wu, L. Liu, J. Peng, Y. Cao, Ultrasensitive and highly stretchable multifunctional strain sensors with timbre-recognition ability based on vertical graphene. *Adv. Funct. Mater.* **2019**, *29*, 1907151.

[11] S. Gong, L. W. Yap, Y. Zhu, B. Zhu, Y. Wang, Y. Ling, Y. Zhao, T. An, Y. Lu, W. Cheng, A soft resistive acoustic sensor based on suspended standing nanowire membranes with point crack design. *Adv. Funct. Mater.* **2020**, *30*, 1910717.

[12] T. S. Dinh Le, J. An, Y. Huang, Q. Vo, J. Boonruangkan, T. Tran, S. W. Kim, G. Sun, Y. J. Kim, Ultrasensitive anti-interference voice recognition by bio-inspired skin-attachable self-cleaning acoustic sensors. *ACS Nano* **2019**, *13*, 13293-13303.

[13] S. Das, R. Singh, A. Das, S. Bag, R. P. Paily, U. Manna, Abrasion tolerant, non-stretchable and super-water-repellent conductive & ultrasensitive pattern for identifying slow, fast, weak and strong human motions under diverse conditions. *Mater. Horiz.* **2021**, *8*, 2851-2858.

[14] Z. Dai, S. Ding, M. Lei, S. Li, Y. Xu, Y. Zhou, B. Zhou, A superhydrophobic and anti-corrosion strain sensor for robust underwater applications. *J. Mater. Chem. A* **2021**, *9*, 15282-15293.